

Article

Experimental Study of a Piezoelectric De-Icing System Implemented to Rotorcraft Blades

Eric Villeneuve ^{1,*} , Sebastian Ghinet ² and Christophe Volat ¹

¹ Anti-Icing Materials International Laboratory (AMIL), Department of Applied Sciences, Université du Québec à Chicoutimi (UQAC), 555 Boulevard de l'Université, Chicoutimi, QC G7H 2B1, Canada; christophe_volat@uqac.ca

² National Research Council Canada, Flight Research Laboratory, Ottawa, ON K1A 0R6, Canada; Sebastian.Ghinet@nrc-cnrc.gc.ca

* Correspondence: eric1_villeneuve@uqac.ca

Abstract: A four-year project investigating the use of piezoelectric actuators as a vibration-based low power de-icing system has been initiated at the Anti-Icing Materials Laboratory. The work done preceding this investigation consisted of studying, numerically and experimentally, the system integration to a flat plate structure, the optimal excitation of the system, the resonant structural modes and the shear stress amplitudes to achieve de-icing for that structure. In this new investigation, the concepts and conclusions obtained on the flat plate structure were used to design and integrate the system into a rotating blade structure. An experimental setup was built for de-icing tests in rotation within an icing wind tunnel, and a finite-element numerical model adapted to the new geometry of the blade was developed based on the expertise accumulated using previous flat plate structure analysis. Complete de-icing of the structure was obtained in the wind tunnel using the developed de-icing system, and its power consumption was estimated. The power consumption was observed to be lower than the currently used electrothermal systems. The finite-elements numerical model was therefore used to study the case of a full-scale tail rotor blade and showed that the power reduction of the system could be significantly higher for a longer blade, confirming, therefore, the relevance of further de-icing investigations on a full-scale tail rotor.

Keywords: icing; wind tunnel; experimental testing; numerical modeling; aerospace; ice protection system; rotorcraft; vibration; piezoelectricity



Citation: Villeneuve, E.; Ghinet, S.; Volat, C. Experimental Study of a Piezoelectric De-Icing System Implemented to Rotorcraft Blades. *Appl. Sci.* **2021**, *11*, 9869. <https://doi.org/10.3390/app11219869>

Academic Editor:
Giuseppe Lacidogna

Received: 3 September 2021
Accepted: 19 October 2021
Published: 22 October 2021

Publisher's Note: MDPI stays neutral with regard to jurisdictional claims in published maps and institutional affiliations.



Copyright: © 2021 by the authors. Licensee MDPI, Basel, Switzerland. This article is an open access article distributed under the terms and conditions of the Creative Commons Attribution (CC BY) license (<https://creativecommons.org/licenses/by/4.0/>).

1. Introduction

In-flight icing is a major problem for rotorcraft, which considerably limits its operations. The most adverse effects come from the aerodynamics of the iced rotor blades, resulting in drag increases and flow separations, which severely affect lift forces [1]. While a few large helicopters use electrothermal ice protection systems, most rotorcraft are not habilitated to fly under icing conditions due to a lack of required protection systems. Electrothermal systems, the only technology currently in use, require too much power to be a viable solution for those small vehicles [2]. Other rotating devices also suffer from the same problem, from small UAS rotors [3,4] to large wind turbines [5–7]. In order to find a low-power alternate solution for smaller rotorcraft, a comprehensive project has been initiated to develop a vibration-based piezoelectric actuator de-icing system, which could also be implemented to other rotating devices. By using piezoelectric actuator elements, the developed system excites a structure at its resonant frequencies to generate sufficient deformation and stresses to break and shed the accumulated ice. This principle is different from other studies which have used piezoelectric actuators to create ultrasonic waves at the ice/substrate interface to generate de-icing [8–11]. Budinger [12,13] also investigated this principle using computational methods to calculate the currents and voltages required to obtain cracking and delamination of the ice at different resonant modes. Similar to this

study, cracking was obtained due to tensile stress, which also leads to the delamination zone following the crack propagation. An ANSYS model was developed by Tian et al. [14], which also demonstrated that delamination is caused by shear stress at the ice/substrate interface and that it is initiated at the edges of the ice layer. Finally, Harvey [15] and Villedeneuve [16] confirmed the validity of this concept by successfully achieving total de-icing of a static actual tail rotor blade structure.

The present study represents an incremental improvement and complexification of previously presented experimental and Finite-Elements Analysis (FEA)-based numerical investigations where the principle of the proposed design method was demonstrated using a simple flat plate structure. The results of these experiments were published in [17–19], where a comprehensive literature study was presented, and the optimal integration and excitation of the actuators, the steady-state and transient vibration response and the stresses involved in icebreaking were extensively studied experimentally and numerically. In this new study, the developed and demonstrated concept was applied to a more complex structure, e.g., a rotating small-scale 22.9 cm (9 inches) long blade setup.

A new experimental setup was designed for testing the piezoelectric de-icing system integrated into a blade in rotation in an icing wind tunnel. An FEA-based numerical model was adapted to the new geometry of the blade, and the new experimental setup was developed based on the expertise accumulated previously. The model was used to determine the frequencies and shape of the structural resonant modes susceptible to generating de-icing of the blade. The FEA-based numerical model was used at several stages of this study, allowing the design of the optimal positioning and excitation of the actuators to investigate shear stresses and obtain useful conclusions. Complete de-icing of the blade was successfully achieved experimentally, and the power consumption of the system showed a reduction compared to electrothermal systems. The numerical model was, therefore, further modified to simulate a full-scale, 0.60 m long, tail rotor blade leading edge, using the information obtained from the small-scale model, and demonstrated that the power reduction could be significantly greater on the full-scale blade, demonstrating the relevance of further developments on a full-scale blade.

2. Materials and Methods

2.1. Refrigerated Wind Tunnel

Testing was performed in the Anti-icing Materials International Laboratory's (AMIL) Icing Wind Tunnel (IWT), shown in Figure 1, which is a closed-loop low-speed refrigerated and thermally-isolated wind tunnel designed to operate at subzero temperatures at sea level pressure. A complete description of AMIL's IWT can be found in [20,21]. The refrigeration system is able to vary and maintain total air temperature between $-48\text{ }^{\circ}\text{C}$ and $22\text{ }^{\circ}\text{C}$. The IWT has two test sections. The larger test section is 0.91 m wide by 0.76 m high, and tests can be performed at airspeeds up to 50 m/s at room temperature. The wind tunnel meets the conditions [22] of the Society of Automotive Engineers (SAE) Aerospace Recommended Practice for icing wind tunnel ARP5905 [23] and Aerospace Information Report for droplets sizing AIR4906 [24]. A water spray system was used to generate the icing cloud. It comprises up to three spray ramps of eight to nine air atomizing nozzles composed of pneumatic sprinklers. A cooling unit controls the water temperature used to produce a cloud of supercooled water droplets with median volumetric diameters (MVD) ranging from 20 to 100 μm and liquid water contents (LWC) ranging from 0.1 to 3.0 g/m^3 . The water is filtered and cleaned to obtain osmotic de-mineralized distilled water. The supercooled droplets impinge on the test model in the center of the test section. During a test, the water flows continually, the air pressure is turned on when the test begins, and the simulated cloud is formed in the IWT test section.



Figure 1. AMIL icing wind tunnel [20].

2.2. Static Small-Scale Blade

The setup is based on a real helicopter tail rotor blade with a NACA 0012 airfoil shape and a 13.1 cm (5.25 inches) chord, as used by industrial partners. The span is limited to 22.9 cm (9 inches) to prevent excessive imbalances in rotation, as well as to fit in the wind tunnel test section used for testing. An aluminum foil 0.8 mm thick, the same thickness as the tail rotor blade's hollow leading edge [16], was given a curved shape to recreate the first 4.5 cm (1.8 in) of a NACA0012 airfoil profile (Figure 2). This section was selected since the leading edge of the blade is where most of the ice accumulation occurs. Aluminum was selected to fabricate a representative NACA0012 shape. It was observed that trying to bend a steel sheet with sufficient precision in order to fabricate the NACA0012 profile in the laboratory would have been very challenging or impossible with the tooling that was readily available. Six piezoelectric actuator patches PI876.A15 were installed on the curved aluminum foil. The patches were 61 mm long by 35 mm wide, with a total thickness of 0.8 mm. They were made of PIC255 piezoelectric materials, a flexible, modified PZT material. The patches were installed along the blade length due to size limitations within the profile (Figure 2). This configuration was selected to allow the installation of the patches within the very limited space in the hollow volume of the profile. For the real tail rotor, the hollow space behind the leading edge is approximately 1 cm [16], and the test setup's hollow dimension was kept as close to this value as possible while allowing the integration of the actuators. Three patches were installed on the upper and lower inner surfaces of the profile. The patches were installed as close as possible to the leading edge in the chord direction, limited by the curvature of the profile, which resulted in a distance of 1.3 cm (0.50 inch) from the leading edge. Spanwise, an actuator was installed centered with the profile on both the top and bottom surface to excite the resonant modes with an odd number of anti-nodes since they all contain an anti-node at the center of the structure. On each side of those actuators, the other actuators were centered in the remaining available space, at 1.14 cm (0.45 inch) from the edges of the profile. Epo-tek 353ND glue, as recommended by the piezoelectric actuator manufacturer, was used to bond the actuators to the structure.

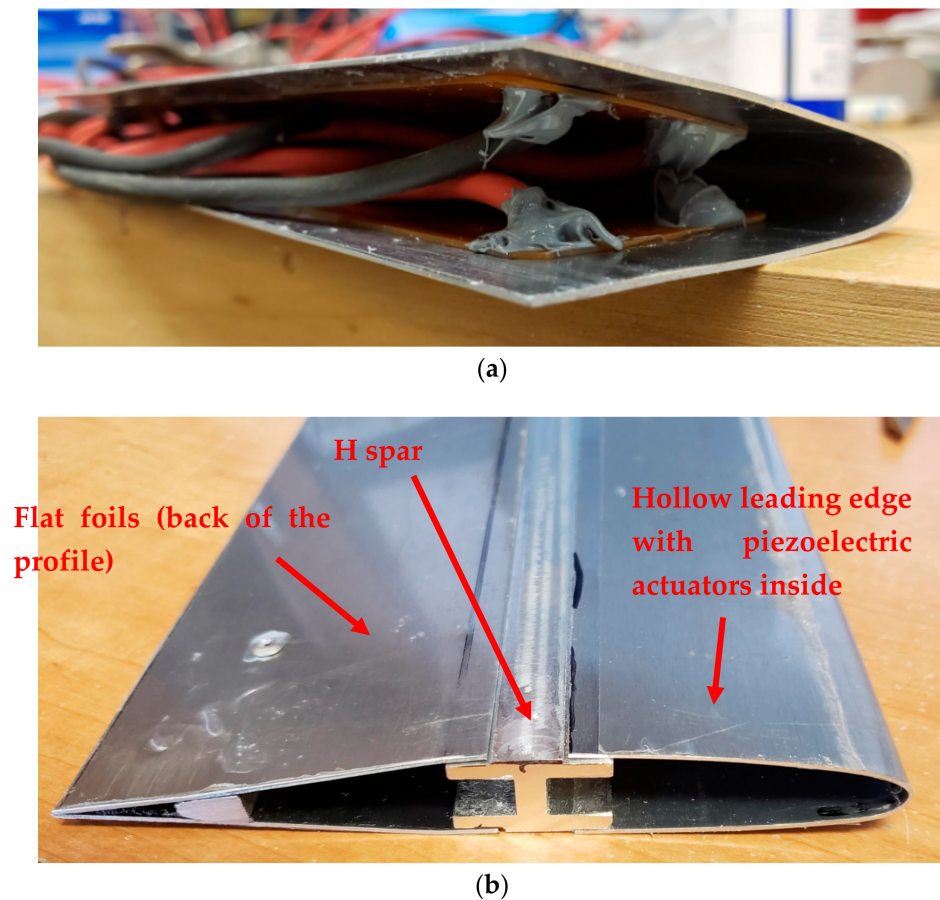


Figure 2. Small-scale blade experimental setup. (a) Leading edge part of the blade setup with piezoelectric actuator patches installed, and (b) assembled profile with leading edge (including piezoelectric actuators), H spar, and back of the profile.

Two additional aluminum plates of the same thickness were used to build the back of the profile. They were shaped to replicate the back of the NACA0012 profile shape. The leading edge and back of the profile were assembled using an H spar (Figure 2). Rivets were used to assemble the parts on the H spar. The maximum number of possible rivets were used for the leading edge to recreate, as closely as possible, a fully clamped boundary condition. The blade structure was held in place in the wind tunnel using two fixation plates on each side of the profile. To operate the piezoelectric actuators, an Agilent 33500B waveform generator was used to provide the electrical driving signal to the actuators. The driving signal for the actuators was amplified using an Amp-line AL-1000-HF-A amplifier with a range of 50 to 1000 V to generate the required vibration level. Since the operational voltage of the actuators is -250 to 1000 V, an Amp-line AL-100DC power source was used to offset the voltage to allow testing at higher voltage swings (higher Vpp). However, when an actuator must be dephased from the other actuators, the positive wire was plugged into the negative output. This means that when an actuator is dephased, a maximum voltage of 500 Vpp can be applied to the actuators due to their voltage limit of -250 V to 1000 V, and only the same offset can be applied to all actuators. The voltage applied to the actuators was measured using a Fluke 105B oscilloscope.

2.3. Rotating Small-Scale Blade

In order to rotate the blade structure, an existing laboratory setup, e.g., the Powered Spinning Rotor Blade (P-SRB) system, was used. This setup has been developed to test active ice protection systems [21]. In more detail, the SRB setup is a horizontal spinning model and is composed of a motor, power shaft transmission, hub, and two blades. The

hub is connected to a 3600 RPM 10 hp motor by a 1 in diameter power steel shaft connected to a 10 hp drive. To safely operate the SRB in the icing wind tunnel (IWT), the test section windows are made of polycarbonate thermoplastic resin (Lexan), which has high impact resistance. The motor generator is computer-controlled and maintains a constant RPM throughout an icing encounter. The spinning rotor blade's angular speed is measured by an optical encoder. The hub is an in-house developed concept with a diameter of 200 mm. The hub allows for two angles of attack for testing: 0° and 6° . An IEC corporation FMA-2-UHF-2FT-SH slip ring is used to bring the power to the rotating blade to excite the actuators. The slip ring voltage range is -500 to 500 V, which limits the voltage of operation for the actuators. The slip ring had 10 channels, which allowed the connection of the six actuators to test the different actuator phasings required. Due to the time and budget limitations, a test dummy of cylindrical shape was built and installed on the second attachment of the hub. The test dummy was fabricated with weights precisely identical to the blade profile in order to minimize the unbalance during rotation. For the conditions tested, the vibration of the blade, due to rotation (flapping), was monitored and found to be at the same levels as the usual vibration obtained, below 1 g, during similar testing performed at the laboratory with different setups, including two identical blades [21]. However, the rotation speed was maintained at 600 RPM to ensure the safe operation of the system and of the multiple wires used to connect the piezoelectric patches and accelerometer. They were connected to the actuators on one end, then tied together and attached to the hands of the hub, as well as to the swivel, to finally be connected to the slip ring to allow power to get through during rotation (Figure 3). This caused the wires to be exposed to the icing environment and attached in a configuration that would make them susceptible to break or disconnect. For these reasons, and since this was part of a first test campaign for this new system with such a large, heavy and complex blade structure, the rotation speed was limited. This design will be largely improved in the near future to allow testing at a higher rotation speed. The final testing setup is shown in Figure 3.

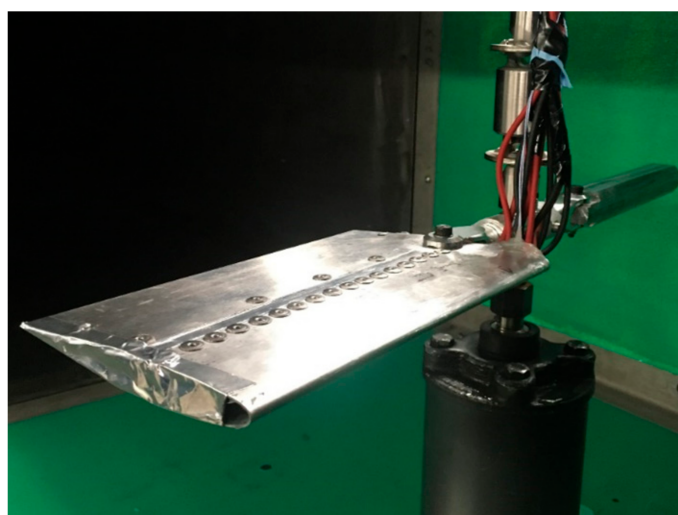


Figure 3. Rotating blade setup in the wind tunnel.

2.4. Test Conditions

The test conditions for the static and rotating wind tunnel tests are presented in Table 1. The conditions were selected to simulate in-flight icing conditions within the limitations of the tunnel. The air temperature was set to obtain a glaze ice accumulation. This results in transparent ice of higher density, usually close to 900 kg/m^3 .

Table 1. Test Conditions.

Test	Wind Speed (m/s)	Air Temperature (°C)	LWC (g/m ³)	MVD (μm)	Rotation Speed (RPM)
Static	20	−7	0.8	20–30	0
Rotating	20	−7	0.8	20–30	600

3. Numerical Model

A similar ABAQUS FEA-based numerical model, as developed and validated in the previous investigations by [17,19], was developed to replicate the structure and boundary conditions of the blade-based testing setup. The blade geometry was designed to replicate as accurately as possible the experimental setup. An extruded shell part was created using NACA0012 coordinates to generate the profile with a chord of 13.3 cm (5.25 in). The NACA profile was cut to 4.5 cm, which corresponds to the vibrating leading-edge part of the experimental setup, known to accumulate most of the ice. The resulting profile was extruded to a span of 22.9 cm (9 in). The thickness of the shell was set to 0.8 mm. Aluminum 2024-T4 material was used, with a mass density of 2780 kg/m³, Young's modulus of 73 GPa and a Poisson's ratio of 0.33. The six actuator patches were modeled using piezoelectric elements with a curved profile to fit the shape of the blade, consistent with the experimental setup (Figure 4). The patches were positioned on the blade part to correspond to their actual position in the physical setup.

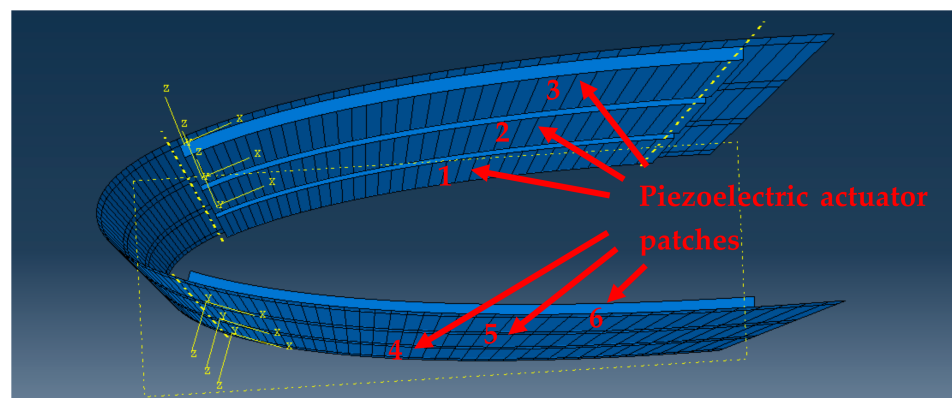


Figure 4. Piezoelectric actuator patches attached to the curved blade shell with their respective identification numbers.

The ice layer was created as a 3D homogenous deformable extrusion in the numerical model. The thickness was set to 6.35 mm (1/4th of an inch)—the limit accepted on the rotorcraft blade in de-icing. Ice material properties were set to a density of 897 kg/m³, Young's modulus of 9 GPa and a Poisson's Ratio of 0.31. The shape of the ice was based on the NACA 0012 airfoil profile as the ice tends to preserve the shape of the leading edge under this accumulation regime (Figure 5). Ice accumulation can be altered due to the rotation of the profile, which is something to consider for the numerical model of the rotating blade. With the increase in tangential velocity along the radius, more ice tends to accumulate at the tip of the blade than at the root. However, experimentation showed that for the low rotation speed and small radius of the rotating blade setup, the rotation had a negligible effect on the ice accumulation and the ice shape was similar to the one obtained during fixed tests (Figure 5b), also showing that the test dummy did not affect the ice accumulation. For this reason, the ice part was not modified for numerical analysis of the rotating setup. A convergence study was performed, and the number of elements was set to 26,400 C3D8R 8-node linear brick elements in the ice layer and 8664 linear S4R shell elements for the profile. To add the effect of rotation, a radial force load was applied to

the ice layer, in an additional general static step, determining the initial pre-strained state for the frequency and direct steady-state dynamic simulations. The force was calculated from the ice mass of 11 g, rotation speed of 600 RPM and average radius of 16 cm, or a total force of 7 N along the radius. Even if this method has not been validated experimentally on its own, it is a commonly used representation [25]. This method allowed a quick and reasonable estimation of the additional shearing provided by the centrifugal force, but a deeper investigation to validate this method experimentally should be completed in a more comprehensive future study. The ice and piezoelectric actuator patches were attached to the blade shell structure using Tie constraints. A fully constrained clamped boundary condition was applied to the back of the profile along the span direction, representing the clamping of the leading edge section to the H-spar in the experimental setup. Frequency and direct steady-state dynamic analyses were conducted with electric potential boundary conditions applied to the actuators for the dynamic analysis.

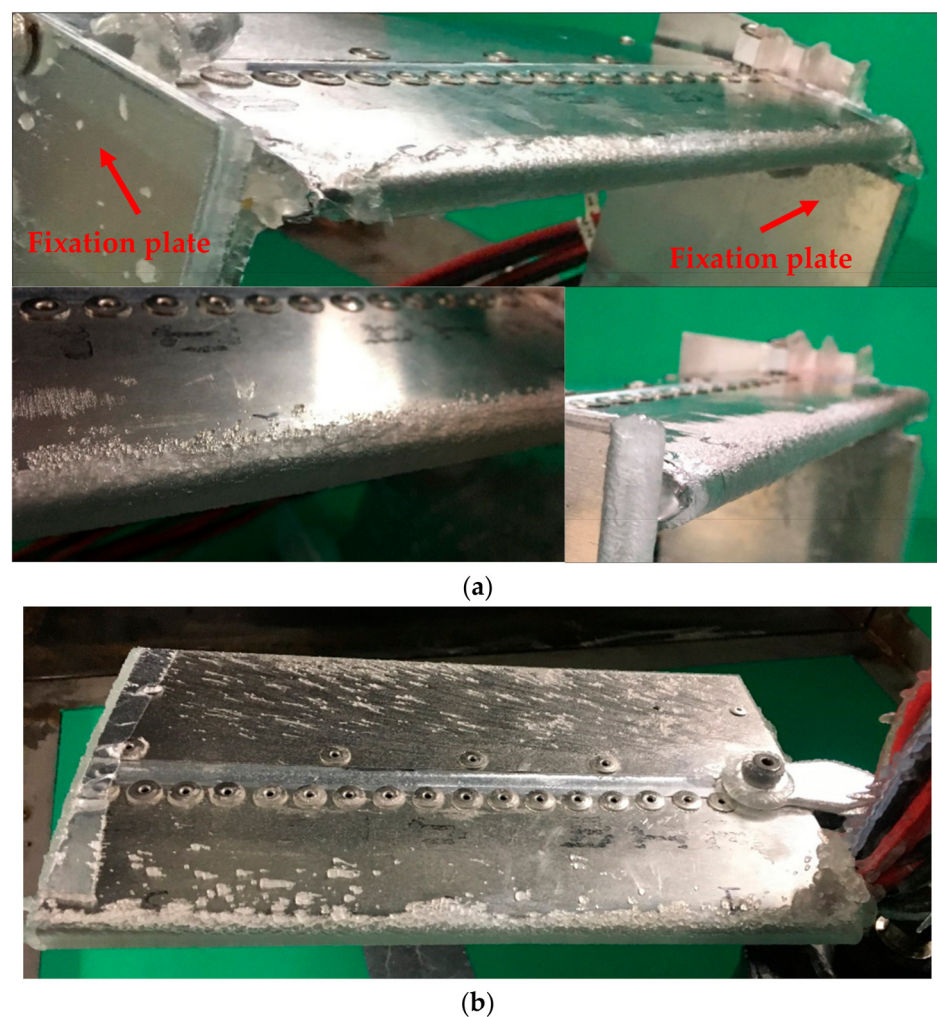


Figure 5. Cont.

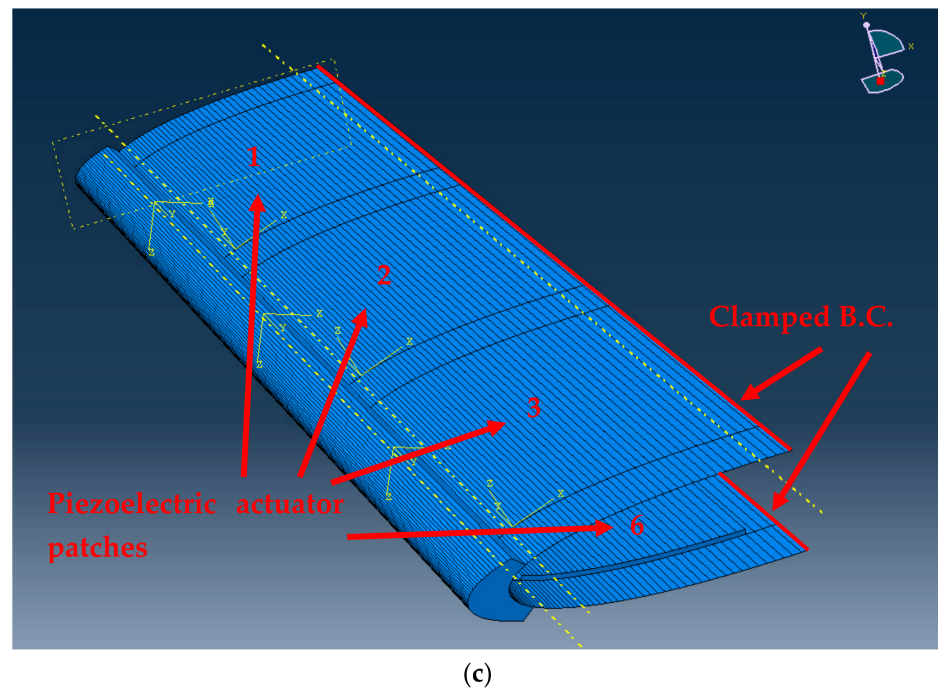


Figure 5. (a) Experimental ice accumulation in static (b) accumulated at 600 RPM rotation speed and (c) numerical model with ice layer.

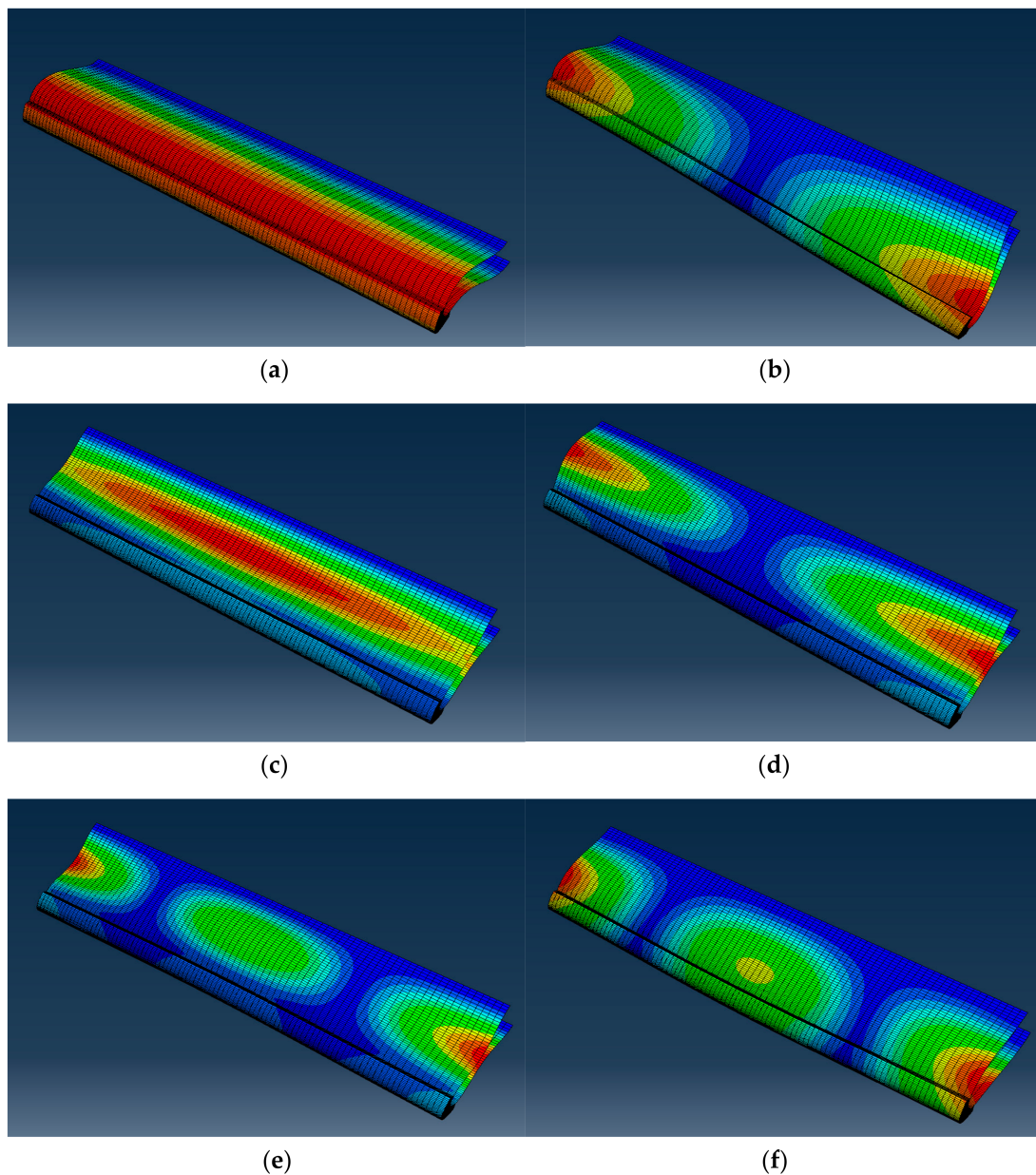
4. Results

4.1. Frequency Analysis

The frequency analysis was performed from 0 to 5 kHz. The modal shapes of the first six predicted modes are presented in Figure 6. The mode shapes presented in Figure 6 are given in the form of the normalized relative displacement and provide a very important indication of how the structure behaves at a natural frequency. These results, the modal frequencies and the mode shapes, were very important, as a qualitative evaluation, in the preliminary setup design stages to decide on the optimal positioning of the actuators and how to operate them, e.g., which actuators should be excited in phase or out of phase and which should simply not be operated at all for each natural frequency of interest. For higher resonant modes, the anti-nodes are smaller than the actuator patches (Figure 7). The position of the first actuator patch is circled in red, showing that the patch overlaps two different anti-nodes. As observed in the previous study on the flat plate [17], an actuator overlapping two anti-nodes resulted in a suboptimal excitation of the resonant mode and when the structure was not optimally excited, the resulting vibration amplitude was weak, and the results of the numerical modeling were less accurate. Moreover, the power consumption increased with an increase in the frequency of excitation since power is linearly dependent on the frequency (see Equation (1)). For these reasons, only the first six resonant modes were studied to achieve the ice layer breaking in this part of the study (Table 2). Rotation did not affect the mode shapes, which was expected due to the very low rotation speed and high rigidity of the clamped leading edge structure, and this is the only vibrating part considered, as opposed to the complete blade.

Table 2. Frequencies of the blade resonant modes with the ice layer calculated with the numerical model.

Mode (#)	Numerical Frequency (Hz)
1	559
2	1136
3	1828
4	1865
5	2038
6	2149

**Figure 6.** First six resonant modes of the blade structure: (a) mode 1 at 559 Hz; (b) mode 2 at 1136 Hz; (c) mode 3 at 1828 Hz; (d) mode 4 at 1865 Hz; (e) mode 5 at 2038 Hz; (f) mode 6 at 2149 Hz.

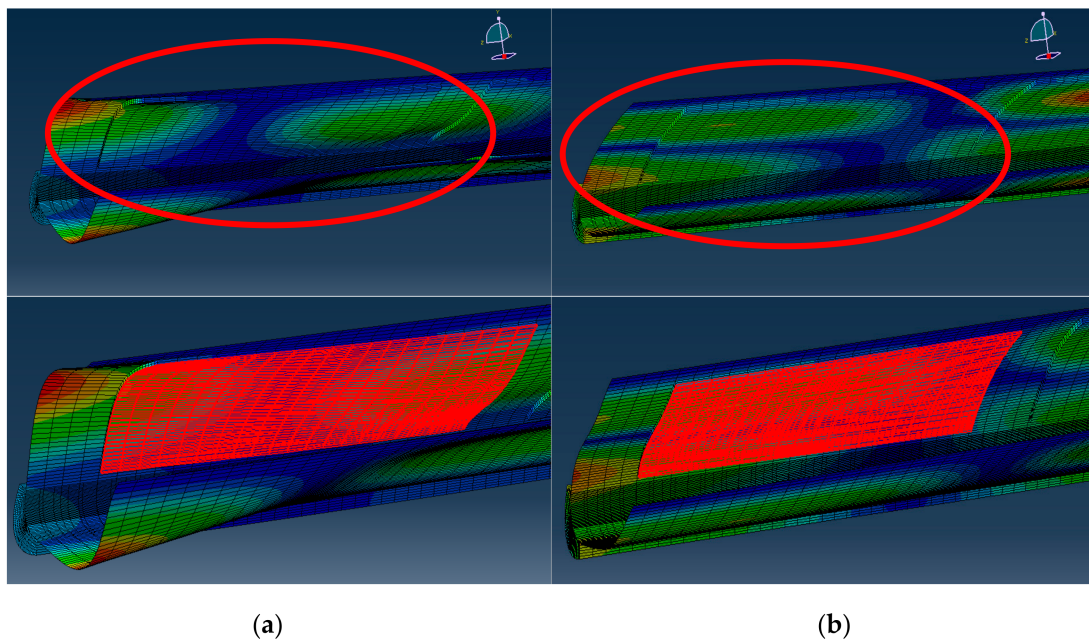


Figure 7. Resonant mode: (a) mode 7 at 2487 Hz and (b) mode 12 at 3340 Hz and position of the actuator patch circled in red (top) and highlighted (bottom) positioned on two different anti-nodes.

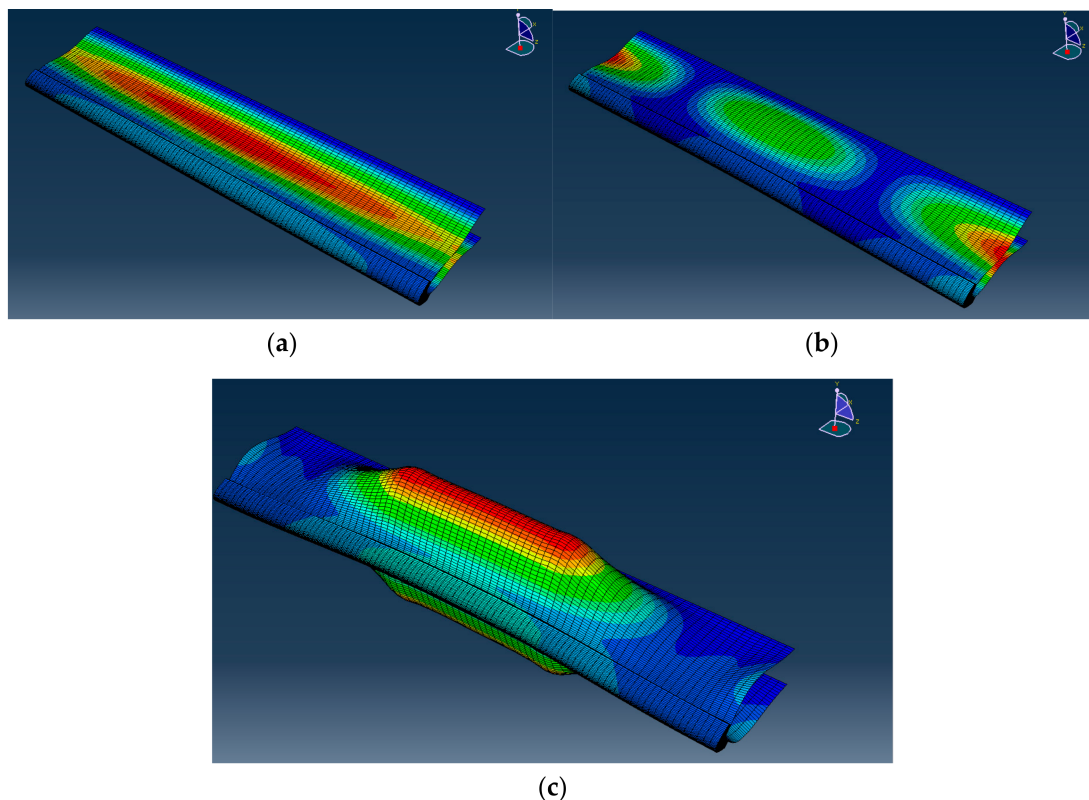
4.2. Static Direct Steady-State Dynamic Analysis

Direct steady-state dynamic numerical analyses were conducted at the natural frequencies calculated using frequency analysis. Experimental icing tests were also performed with the blade setup under static (without blade rotation) mode with an ice layer accumulation for each of the modes. For each mode, the optimal actuator phasing excitation was used for numerical simulations and testing. Table 3 presents the optimal phasing for each natural mode as well as the voltage range within which delamination was predicted by the model. The piezoelectric actuators attached to the inside upper surface of the profile from left to right are identified as 1 to 3, while the actuator patches, from left to right, attached to the inside of the lower surface of the profile were identified as 4 to 6 (Figures 4 and 5b). Actuators on the same side of the backlash are all excited identically, at the same voltage and in phase. However, they are excited, at the same voltage, and in counter phase with the actuators on the other side of the backlash. The ice delamination is predicted to be achieved when the calculated numerical shearing stress values at the ice substrate interface are within the yield limit range defined during experiments with the flat plate and validated in the literature, as detailed in [19]. The voltage range corresponds to the voltage required to achieve the stress range defined previously. As explained in Section 2.3, a maximum of 500 Vpp can be applied without compromising the integrity of the actuators when not all the actuators are excited in phase. Testing was conducted by performing a frequency sweep at a low sweep rate (below 70 Hz/s) around the target frequencies and slightly increasing the voltage between each sweep until delamination was obtained or maximum voltage was reached. Delamination was obtained experimentally when the structure was excited using the actuator patches for modes 5 and 6, as presented in Table 3, while mode 3 could not be excited due to the form of the mode shape and the disposition of the piezoelectric patches.

Table 3. Actuator excitation and numerical voltage for ice delamination.

Mode (#)	Optimal Actuator Phasing	Predicted Voltage for Delamination (Vpp)	Delamination Obtained at 500 Vpp and Below
1	1-2-3/4-5-6	>800	No
2	1-6/3-4	>700	No
3	1-2-3-4-5-6	>500	No
4	1-4/3-6	425 to 1950	No
5	1-3-4-6/2-5	250 to 1100	Yes
6	1-3-5/2-4-6	540 to 2500	Yes

For the third mode, the optimal actuator excitation is defined by all in-phase actuators (Figure 6c). With this activation, the numerical model results showed that the piezoelectric actuators would not properly excite the structure. As expected, the mode deployment only partially corresponds to the third resonant mode shape (Figure 8) but is largely affected by the geometrical disposition of the patches. The piezoelectric d_{31} effect, which represents the directions of the mechanical strain experienced by the actuator from the application of an electric field, creates a deformation of the actuators in both directions, as shown in Figure 9. With the greater deformation generated over the length, the actuators at the center create more of an anti-node corresponding to that of the middle anti-node of mode 5. If the actuators were positioned in the perpendicular direction, their deformation would have favored bending, mostly in the direction proper to mode 3 generation. However, due to size restrictions, it was not possible to accommodate the patches positioning. This demonstrates that, experimentally, while mode 5 could be excited, mode 3 would not. This was also confirmed experimentally since no distinct resonant mode was observed around the natural frequency corresponding to the third mode, only for mode 5.

**Figure 8.** Frequency analysis of (a) mode 3 and (b) mode 5, and (c) direct steady-state dynamics analysis for mode 3.

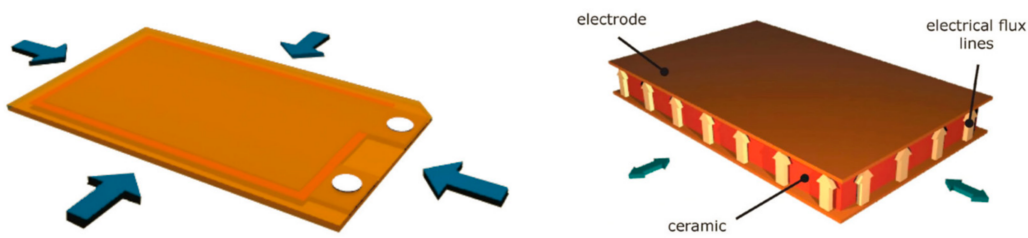


Figure 9. Lateral contraction and d_{31} effect [26].

Delamination was obtained experimentally for modes 5 and 6. Multiple test runs were performed for those two modes to assess the repeatability of the experiment. The numerical investigation showed that with all piezoelectric actuators excited in phase, mode 5 could be excited due to the geometry and bending properties of the actuator patches. Two additional icing tests were performed with this excitation configuration to verify the hypothesis. Similar to the results obtained for mode 5, the geometry and bending of the actuators should allow the proper excitation of mode 6 with actuators 1, 2 and 3 out of phase with regard to the actuators 4, 5 and 6. Testing with this phasing was successfully performed. The experimental voltage obtained at delamination is presented in Table 4. An example of delamination is presented in Figure 10. Delamination (before detachment) is identified by a white air-filled zone observed under the ice layer.

Table 4. Experimental voltage for ice delamination.

Mode (Repetition)	Actuator Phasing	V _{pp} (V)
5 (1)	1-3-4-6/2-5	336
5 (2)		352
5 (1)	1-2-3-4-5-6	370
5 (2)		352
6 (1)	1-3-5/2-4-6	385
6 (2)		400
6 (3)		385
6 (1)		450



Figure 10. Delamination at 352 V_{pp} for mode 5, repetition 2, with all piezoelectric actuators excited in phase.

4.3. Rotating Blade

For the rotating blade experiments, tests were performed at the conditions described in Section 2.3 for the angles of attack of 0° and 6° , respectively. The small difference in angle of attack resulted in a very similar ice accumulation at the leading edge (Figure 11). The only difference was observed underneath the profile, where a very thin layer of brittle ice was accumulated.

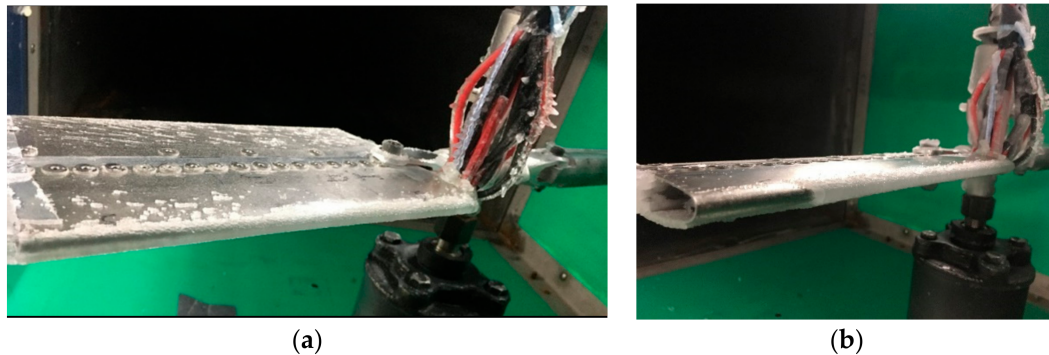


Figure 11. Ice layer at (a) 0° AOA and (b) 6° AOA.

Delamination was obtained for only two modes during static (without blade rotation) tests. In rotation, frequency sweeps at low sweep rates (below 70 Hz/s) up to 4000 Hz were first performed to assess if and at what frequencies a completed de-icing of the ice layer could occur. Due to voltage offsetting, the voltage was limited to 500 Vpp for all actuator phasing tests, except with all actuators excited in phase. The voltage phasing configurations tested in rotation were the same as for the static (without blade rotation) tests (see Section 4.2). For the phasing configurations where the voltage was limited to 500 Vpp, no de-icing could be obtained. The very low rotation speed and small radius of the setup did not generate sufficient force to help the system de-ice the profile. When all piezoelectric actuators were activated in phase, the voltage could be increased up to 750 Vpp, from -250 V to 500 V, by offsetting the voltage to 125 V. At this higher voltage, de-icing was obtained at the frequency corresponding to mode 5. De-icing tests were repeated for this configuration (sweeping frequency of mode 5, all actuators in phase) four times at a 6° angle of attack (AOA). At 0° , during the third test, a connection to the actuator broke, and tests had to be stopped. Table 5 presents the voltage at de-icing in rotation. De-icing results were similar at the 0° and 6° angles of attack (AOA), which was expected due to the similarities in ice accumulation. Complete de-icing of the leading edge was obtained for all tests performed. In most tests, complete delamination and ice shedding were obtained after two consecutive frequency sweeps around the resonant mode. During the first sweep, de-icing of the first and last thirds of the blade's leading edge occurred, and de-icing of the center of the blade occurred during the second sweep (Figure 12). In one of the tests, de-icing of the first two-thirds of the blade was obtained during the first sweep (Figure 13a), and de-icing of the rest of the blade occurred during the second sweep (Figure 13b). The results were similar at 0° and 6° . However, due to the angle of attack, a slightly longer ridge of ice was obtained under the profile at 6° .

Table 5. Experimental results for rotating setup.

AOA (Repetition)	Vpp (V)
0 (1)	660
0 (2)	650
6 (1)	680
6 (2)	680
6 (3)	660
6 (4)	680

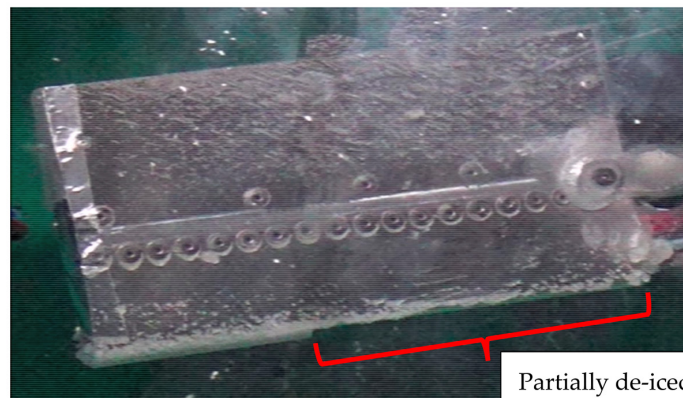


(a)



(b)

Figure 12. (a,b) Complete de-icing after a test at 6° AOA.



(a)



(b)

Figure 13. (a) Partial de-icing after first sweep and (b) complete de-icing after second sweep.

5. Discussion on the Small-Scale Blade Results

5.1. Experimental Variability

The experimental variability was calculated from the different test repetitions performed in the wind tunnel. For mode 5, the frequency input into the actuators following delamination varied by 8% in static test conditions. For both excitation cases, with actuators 1, 3, 4 and 6 out of phase compared to the actuators 1 and 2, and with all actuators in phase, the delamination voltage varied by 2%. For mode 6, the delamination was obtained within a 2% frequency variation and the voltage by a maximum variation of 3%. For the rotating setup, tests were performed at 0° and 6° AOA. The results were similar, except for the ridge of ice on the lower surface of the profile, and the results were considered as a single test condition for the analysis. The frequency at de-icing varied by 10% between all the test repetitions performed, and the voltage by 3%. The resulting variation is presented in Table 6, and the maximum variation obtained was 10%.

Table 6. Percentage of variation for static and rotating experimental testing for modes 5 and 6.

Mode	Excitation	Frequency	V _{pp}
5	1-3-4-6/2-5	8%	2%
	1-2-3-4-5-6		2%
	1-2-3-4-5-6 in rotation	10%	3%
6	1-3-5/2-4-6	2%	3%
	1-2-3/4-5-6		N/A

5.2. Numerical Model Stress Prediction

Experimental validation of the numerical model could not be performed due to the need for developing a proper measurement system to scan the vibration level over the surface of the blade when iced in the wind tunnel, which is a complex task on its own. The numerical model developed for this task allowed us to draw very useful conclusions to show that the behavioral trends of the model are accurate and that the model can be used for comparative study. Table 7 shows the shear stress calculated using the numerical model. The numerical model prediction for delamination was between 0.20 and 0.35 MPa, which was in the 0.20 to 0.90 MPa range obtained previously [19], meaning that the numerical model stress predictions are in accordance with what was obtained using the flat plate setup. No cracking, only delamination, of the ice layer was predicted by the numerical model and no cracking, only delamination was obtained experimentally.

Table 7. Shear stresses calculated by the numerical model in static.

Mode (Repetition)	S ₁₂ (MPa)
5 p * (1)	0.27
5 p * (2)	0.30
5 (1)	0.26
5 (2)	0.35
6 p * (1)	0.33
6 p * (2)	0.32
6 p * (3)	0.22
6 (1)	0.20

* with optimally-phased actuators.

For the experimental tests, including blade rotation, the calculated stress is presented in Table 8. The shear stresses predicted by the numerical model were higher than for the static tests. Those values estimated the shear stress limit for de-icing and shedding of the ice from the surface and not simply delamination. To de-ice the blade structure in rotation, the model predicted a shear stress range of 2.60 to 2.84 MPa.

Table 8. Shear stresses calculated by the numerical model in rotation.

AOA (Repetition)	S12 (MPa)
0 (1)	2.65
0 (2)	2.60
6 (1)	2.84
6 (2)	2.66
6 (3)	2.82
6 (4)	2.69

However, the preliminary investigation demonstrated the methods' robustness on the flat plate setup and the successful implementation in a more complex setup, even if it highlighted that more work is required to optimize the testing setup and improve the numerical models. The numerical model was useful to design and implement the system to the structure, to properly excite the actuators and to predict resonant frequencies, modal shapes and delamination. For the shear stress prediction, the numerical model of the blade was consistent with the flat plate model in predicting delamination. In rotation, the calculated shear stress corresponded to the stress for de-icing and shedding of the ice layer from the blade. The value predicted by the model was 3 to 8 times higher than for simple delamination.

5.3. Power Consumption

The power consumption of the system for the de-icing of the blade setup was calculated using the following formula:

$$P_m = C * f * U_h^2 \quad (1)$$

with P_m being the average electrical power, C the actuator electrical capacitance, f the frequency of excitation and U_h the voltage swing. The electrical capacitance of the actuators was 45 nF. The average frequency of excitation obtained during the de-icing test was 2495 Hz, and the average voltage swing was 668 Vpp. At those conditions, the average power consumption of an actuator was 50 W, meaning a total average power for the six actuators of 300 W. To compare with thermal de-icing systems, the power density is calculated. The common practice is to consider the first 30% of the chord of the profile to calculate the de-iced area [8], corresponding to approximately 15% of its surface area. For this blade setup, an iced zone of 22.9 cm (9 in) spanwise by 4.1 cm (1.6 in) chordwise was considered, for a total of 93.9 cm² (14.5 in²), which results in an average power density of 32 kW/m² (21 W/in²). When compared to 39 to 43 kW/m² (25–28 W/in²) [27] for a thermal de-icing system, this results in a power reduction of up to 25%. While interesting, this power reduction is small enough to justify the implementation of such a complicated system. The blade profile was very small, especially compared to the actuator size. With a longer profile spanwise, it is believed that the blade should have higher flexibility, and vibration would be favored. Moreover, the actuators used in this study would be more fit to be anti-nodes of the first vibration modes for a longer blade, since the ideal length of an actuator corresponds to the size of the anti-node, and larger actuators diminish the efficiency of the system [17], resulting in a more efficient excitation of the structure. Finally, the very low angular speed at which the de-icing tests were performed, as well as the small radius of rotation, did not yield tangential speeds representative of the reality. With higher tangential speeds, higher centrifugal forces would have facilitated de-icing. All these factors would contribute to reduce the power consumption of the system.

6. Full-Length Tail Rotor Leading Edge Numerical Case

Complete de-icing was achieved with the small blade setup. It was concluded, however, that the small span of the structure, the large size of the actuators and very low

rotation speed and radius were factors negatively impacting the power consumption of the system. To test this theory, the numerical model was used to model a full-sized tail rotor leading edge. With its longer span, the flexibility of the structure should favor the vibrations, and the anti-nodes size should be better suited for the size of the piezoelectric patches used in this project. Moreover, a longer span increases the centrifugal force on the ice layer for the same rotation speed. The same extruded shell NACA0012 part cut to 0.045 m used for the small blade model was used for this model. The sketch profile was extruded to a span of 0.60 m, and the thickness of the shell was kept to 0.8 mm. The material was changed to stainless steel, which is the material used to build the real tail rotor. The same mesh elements and element size were used. Fully constrained clamped boundary conditions were also added to the side of the profile, in addition to the one at the back of the profile. These boundary conditions simulate the capping at each end of the blade.

The ice layer was created as a 3D homogenous deformable extruded part. Ice material properties were kept the same as for the other numerical models. The shape of the ice was based on the ice shape obtained with the small blade model, and the thickness was set to 6.35 mm (1/4th of an inch) at the tip of the blade. However, the ice layer is susceptible to having a linear thickness decrease along its span towards its root due to the increase in tangential velocity with the increase in radius [16,21]. To model that phenomenon, the thickness was linearly reduced to 1 mm at the root of the blade (Figure 14). The ice was tied to the blade shell structure using a Tie constraint. The element used to mesh the ice was changed to a C3D10 10-node quadratic tetrahedron. Tetrahedral elements can fit more complex geometries but require more elements to obtain the same accuracy. The element size was increased by a factor of six to compensate for this.

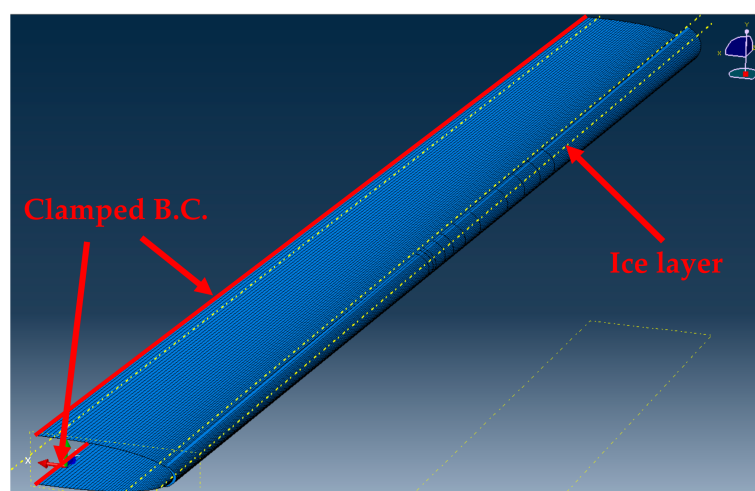
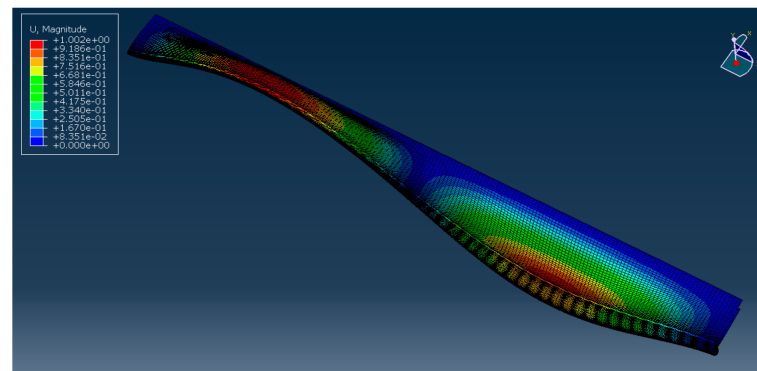


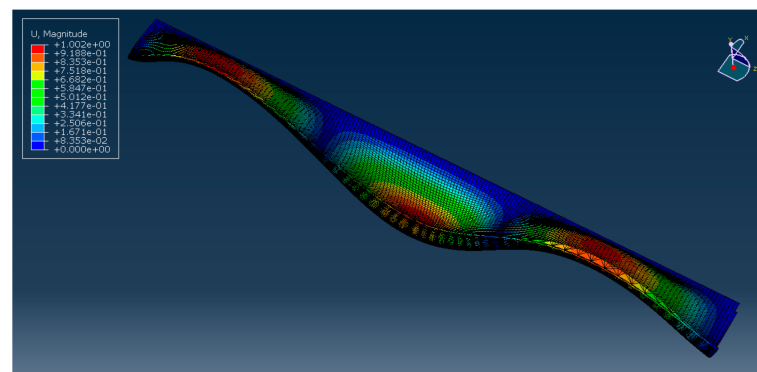
Figure 14. Ice layer part with linear thickness increase.

6.1. Frequency and Direct Steady-State Dynamical Analysis

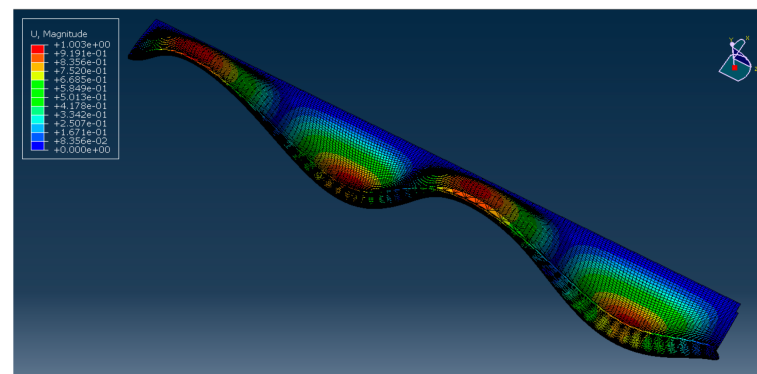
A frequency analysis was first conducted to calculate the first resonant modes of the iced leading edge. As for the small blade setup, the first modes were targeted to minimize power consumption (Equation (1)). Modes 2, 3 and 4 (Figure 15) were selected for their lower frequency and mode shape similar to the successful resonant modes with small blade setup and proper anti-node size for the actuators. Mode 1 was not selected since its mode shape did not correspond to the resonant modes that yielded de-icing with the small blade. While it is possible that this mode is effective, it was preferable to focus on a mode shape similar to those proven effective during experimental testing.



(a)



(b)



(c)

Figure 15. Full-length tail rotor leading edge resonant modes 2 (a), 3 (b) and 4 (c).

For each of those modes, PI876.A15 piezoelectric actuator patches were positioned at the center of each anti-node on the upper and lower surface. The direct steady-state dynamic analysis was conducted for each mode with the optimal phasing of the actuators. For each mode, the voltage peak to peak required to obtain 2.72 MPa of shear stress S12 was determined using the numerical simulation. This corresponded to the average shear stress calculated with the numerical model at complete de-icing of the blade for the small blade setup. Table 9 presents the resonant mode frequencies as well as the voltage values required for each mode to obtain sufficient stress for de-icing in the static case (only the piezoelectric actuator de-icing system) and for the case when a centrifugal force is added. The centrifugal force is considered at 600 RPM, the same as for the small-scale tests and conservative tail rotor rotation speeds, the estimated accumulated ice mass of 25 g and a radius of 0.55 m.

Table 9. Voltage prediction by the numerical model to obtain similar stress at de-icing for the small blade setup.

Mode	Frequency (Hz)	Voltage for Shear Stress = 2.72 MPa (Vpp)	Voltage for Shear Stress = 2.72 MPa in Rotation (Vpp)
2	1015	3510	2500
3	1373	453	323
4	1798	286	205

6.2. De-Icing Scenarios and Power Estimation

The voltage required for de-icing, based on the shear stress obtained with the small blade setup was estimated numerically for the full-length tail rotor case for modes 2, 3 and 4. This setup was used to estimate the power consumption of the system, as detailed under Section 5.3. For the power density calculation, the span was changed from 22.9 cm (9 inches) to 60 cm (23.6 inches) for a 246 cm² (37.8 in²) surface. Table 10 presents the number of actuators used in the numerical model for each mode (one at each anti-node), the total power required to excite the system (all actuators) and reach sufficient stress for de-icing, with and without rotation, as well as the power density and potential power reduction of the system as compared to electrothermal systems. The power density and power reduction are estimated in the same manner as in Section 5.3 for the small-scale blade profile. These values are simple basic estimates based on the various assumptions presented in the previous section and should be considered likewise. These values represent best-case scenarios within the potential voltage range. Furthermore, the exact shedding mechanisms were not fully investigated, and the de-icing prediction was based only on the maximum shear stress prediction by the numerical model. Finally, this is for a hollow leading edge of 4.5 cm, which is significantly longer than the 1 cm hollow leading edge found in the real size tail rotor blade. Despite this, the obtained results showed the power reduction potential and validated the conclusions that power density should be much lower for a larger blade. Power densities down to 1.1 kW/m² (0.72 W/in²) were estimated, which would be a significant improvement. Compared to the value found in the literature, this shows great potential for the system. Despite the important considerations that must be taken into account when judging those values, this potential reduction demonstrates the relevance of deeper investigations on the piezoelectric actuator system integrated into a full tail rotor blade.

Table 10. De-icing power estimation based on numerical prediction for full-length tail rotor leading edge.

Mode	Number of Actuators	Power without Rotation (W)	Power in Rotation (W)	Power Density in Rotation (W/in ²)	Reduction from Thermal System (%)
2	4	2250	1140	30	−8
3	6	76	39	1.03	96
4	8	53	27	0.72	97

7. Conclusions

This study discussed the design and preliminary testing of a piezoelectric de-icing system applied to a small rotating blade. The experimental tests conducted with the test setup were successful, and complete de-icing of the blade was achieved. Power consumption was calculated and showed a 25% reduction as compared to electrothermal systems. An FEA-based numerical model was also developed and used to investigate stresses. The numerical model allowed us to design the optimal positioning and excitation of the actuators to investigate shear stresses and conduct comparative studies. It was then estimated that the power reduction could be much more significant for a longer blade similar to a real tail rotor blade due to the size of the actuators, greater flexibility and higher centrifugal force. The numerical model was modified to the actual span of a real tail rotor,

and the first resonant modes were investigated. The numerical results have confirmed those assumptions, predicting a power reduction of up to 97%. Even if these results are preliminary and based on different assumptions and simplifications, they still show the great potential of the method.

Following this comprehensive investigation on the use of piezoelectric actuators for ice protection systems, it is recommended to pursue the investigation with a full tail rotor prototype. In order to do so, the first step recommended is to use the FEA-based numerical model for the design of new optimal piezoelectric actuators. It is also recommended to design a measurement and operation system for the testing and validation of a full tail rotor prototype. The exact shedding mechanisms were not fully investigated, and the de-icing prediction was based only on the maximum shear stress prediction by the numerical model. While it was successful as a first step, with results for cracking and delamination within the literature values, a more complex approach should, however, be considered for full ice shedding. This kind of excitation could impact the fatigue life of the structure and its aeroelastic stability. This should be investigated in a future study, as well as the durability of the system itself. Finally, the centrifugal force, as defined in the numerical model should be investigated to ensure the validity of the results and could be verified experimentally on its own. This could be done using the Spinning Rotor Blade setup in the wind tunnel without any other systems involved. The stresses involved could then be compared and validated.

Author Contributions: Conceptualization, E.V.; methodology, E.V.; validation, E.V. and S.G.; formal analysis, E.V.; investigation, E.V., S.G. and C.V.; data curation, E.V. and S.G.; writing—original draft preparation, E.V.; writing—review and editing, S.G. and C.V.; supervision, E.V., S.G. and C.V.; project administration, E.V. and C.V.; funding acquisition, C.V. All authors have read and agreed to the published version of the manuscript.

Funding: This research was funded jointly by the CRIAQ/CARIC (grant No. ENV-702), CRSNG (grant No. CRD 478088-14), Bell Textron and Socomore.

Institutional Review Board Statement: Not Applicable.

Informed Consent Statement: Not Applicable.

Data Availability Statement: None.

Conflicts of Interest: The authors declare no conflict of interest.

References

1. Flight Safety Foundation. Inflight Icing and the Helicopter—Results of a U.S. Army investigation into the unique hazards facing rotary wing operations in the winter environment offers timely tips for all helicopter flight crews. *Helicopter Saf.* **1990**, *16*, 4.
2. Coffman, H.J., Jr. Helicopter Rotor Icing Protection Methods. *J. Am. Helicopter. Soc.* **1987**, *32*, 34–39. [[CrossRef](#)]
3. Liu, Y.; Li, L.; Ning, Z.; Tian, W.; Hu, H. Experimental investigation on the dynamic icing process over a rotating propeller model. *J. Propuls. Power* **2018**, *34*, 933–946. [[CrossRef](#)]
4. Liu, Y.; Li, L.; Chen, W.; Tian, W.; Hu, H. An experimental study on the aerodynamic performance degradation of a UAS propeller model induced by ice accretion process. *Exp. Therm. Fluid Sci.* **2019**, *102*, 101–112. [[CrossRef](#)]
5. Han, Y.; Palacios, J.; Schmitz, S. Scaled ice accretion experiments on a rotating wind turbine blade. *J. Wind Eng. Ind. Aerodyn.* **2012**, *109*, 55–67. [[CrossRef](#)]
6. Hann, R.; Hearst, R.J.; Sætran, L.R.; Bracchi, T. Experimental and numerical icing penalties of an S826 airfoil at low reynolds numbers. *Aerospace* **2020**, *7*, 46. [[CrossRef](#)]
7. Wang, Y.; Jiang, X. Design Research and Experimental Verification of the Electro-Impulse De-Icing System for Wind Turbine Blades in the Xuefeng Mountain Natural Icing Station. *IEEE Access* **2020**, *8*, 28915–28924. [[CrossRef](#)]
8. Overmeyer, A.; Palacios, J.; Smith, E. Ultrasonic De-Icing Bondline Design and Rotor Ice Testing. *AIAA J.* **2013**, *51*, 2965–2976. [[CrossRef](#)]
9. Palacios, J.L.; Smith, E.C.; Rose, J.L. Investigation of an Ultrasonic Ice Protection System for Helicopter Rotor Blades. In Proceedings of the 64th Annual Forum Proceedings—AHS International, Montreal, QC, Canada, 29 April–1 May 2018; pp. 609–618.

10. Zhu, Y.; Palacios, J.L.; Rose, J.L.; Smith, E.C. Numerical Simulation and Experimental Validation of Tailored Wave Guides for Ultrasonic De-Icing on Aluminum Plates. In Proceedings of the 51st AIAA/ASME/ASCE/AHS/ASC Structures, Structural Dynamics and Materials Conference [2010–3043] (Collection of Technical Papers—AIAA/ASME/ASCE/AHS/ASC Structures, Structural Dynamics and Materials Conference), Orlando, FL, USA, 12–15 April 2010.
11. Daniliuk, V.; Xu, Y.; Liu, R.; He, T.; Wang, X. Ultrasonic de-icing of wind turbine blades: Performance comparison of perspective transducers. *Renew. Energy* **2020**, *145*, 2005–2018. [[CrossRef](#)]
12. Budinger, M.; Pommier-Budinger, V.; Bennani, L.; Rousset, P.; Bonaccorso, E.; Dezitter, F. Electro-mechanical Resonant Ice Protection Systems: Analysis of Fracture Propagation Mechanisms. *AIAA J.* **2018**, *56*, 4412–4422. [[CrossRef](#)]
13. Pommier-Budinger, V.; Budinger, M.; Rousset, P.; Dezitter, F.; Huet, F.; Wetterwald, M.; Bonaccorso, E. Electro-mechanical Resonant Ice Protection Systems: Initiation of Fractures with Piezoelectric Actuators. *AIAA J.* **2018**, *56*, 4400–4411. [[CrossRef](#)]
14. Bai, T.; Zhu, C.; Miao, B.; Li, K.; Zhu, C. Vibration de-icing method with piezoelectric actuators. *J. Vibroeng.* **2015**, *17*, 61–73.
15. Harvey, D. *Modélisation Numérique d'un Système de Protection Contre le Givre par Éléments Piézoélectriques Avec Validation Expérimentale*; Département des Sciences Appliquées; Université du Québec à Chicoutimi: Chicoutimi, QC, Canada, 2012; p. 297.
16. Villeneuve, E.; Harvey, D.; Zimcik, D.; Aubert, R.; Perron, J. Piezoelectric De-Icing System for Rotorcraft. *J. Am. Helicopter Soc.* **2015**, *60*, 12. [[CrossRef](#)]
17. Villeneuve, E.; Volat, C.; Ghinet, S. Numerical and experimental investigation of the design of a piezoelectric de-icing system for small rotorcraft part 1/3: Development of a flat plate numerical model with experimental validation. *Aerospace* **2020**, *7*, 62. [[CrossRef](#)]
18. Villeneuve, E.; Volat, C.; Ghinet, S. Numerical and experimental investigation of the design of a piezoelectric de-icing system for small rotorcraft part 2/3: Investigation of transient vibration during frequency sweeps and optimal piezoelectric actuator excitation. *Aerospace* **2020**, *7*, 49. [[CrossRef](#)]
19. Villeneuve, E.; Volat, C.; Ghinet, S. Numerical and Experimental investigation of the design of a piezoelectric de-icing system for small rotorcraft part 3/3: Numerical model and experimental validation of vibration based de-icing of a flat plate structure. *Aerospace* **2020**, *7*, 54. [[CrossRef](#)]
20. Samad, A.; Villeneuve, E.; Morency, F.; Volat, C. A numerical and experimental investigation of the convective heat transfer on a small helicopter rotor test setup. *Aerospace* **2021**, *8*, 52.
21. Villeneuve, E.; Blackburn, C.; Volat, C. Design and Development of an Experimental Setup of Electrically Powered Spinning Rotor Blades in Icing Wind Tunnel and Preliminary Testing with Surface Coatings as Hybrid Protection Solution. *Aerospace* **2021**, *8*, 98. [[CrossRef](#)]
22. Villeneuve, E.; Perron, J. *Icing Wind Tunnel Certification Tests in Accordance with SAE ARP5905 and AIR4906*; AMIL: Chicoutimi, QC, Canada, 2012; p. 80.
23. *Calibration and Acceptance of Icing Wind Tunnels*; SAE International: Warrendale, PA, USA, 2003.
24. *Droplet Size Instrumentation Used in Icing Facilities*; SAE International: Warrendale, PA, USA, 1995.
25. Hayashi, R.; Yamamoto, M. Numerical Simulation on Ice Shedding Phenomena in Turbomachinery. *J. Energy Power Eng.* **2015**, *9*, 8.
26. *DuraAct Patch Transducer Datasheet*; Physik Instrumente: Karlsruhe, Germany, 2012.
27. Goraj, Z. An Overview of the Deicing and Antiicing. In Proceedings of the 24th International Congress of the Aeronautical Sciences, Yokohama, Japan, 29 August–3 September 2004.